Substrate rigidity modulates traction forces and stoichiometry of cell–matrix adhesions

Balcioglu, H.E.; Harkes, R.; Danen, E.H.J.; Schmidt, T.

The Journal of Chemical Physics

Substrate rigidity modulates traction forces and stoichiometry of cell–matrix adhesions

Cite as: J. Chem. Phys. **156**, 085101 (2022); https://doi.org/10.1063/5.0077004
Submitted: 29 October 2021 • Accepted: 25 January 2022 • Accepted Manuscript Online: 31 January 2022 • Published Online: 22 February 2022

Hayri E. Balcioglu, Rolf Harkes, Erik H. J. Danen, et al.

The Journal of Chemical Physics ARTICLE scitation.org/journal/jcp

Substrate rigidity modulates traction forces and stoichiometry of cell–matrix adhesions

Cite as: J. Chem. Phys. 156, 085101 (2022); doi: 10.1063/5.0077004
Submitted: 29 October 2021 • Accepted: 25 January 2022 •
Published Online: 22 February 2022

Hayri E. Balcioglu,[1] Rolf Harkes,[2] Erik H. J. Danen,[1,a)] and Thomas Schmidt[2,a)]

AFFILIATIONS

[1] Leiden Academic Center for Drug Research, Leiden University, Leiden, The Netherlands
[2] Physics of Life Processes, Kamerlingh Onnes-Huygens Laboratory, Leiden University, Leiden, The Netherlands

Note: This paper is part of the JCP Special Topic on the Ever-Expanding Optics of Single-Molecules and Nanoparticles.
[a)] **Authors to whom correspondence should be addressed:** e.danen@lacdr.leidenuniv.nl and schmidt@physics.leidenuniv.nl

ABSTRACT

In cell–matrix adhesions, integrin receptors and associated proteins provide a dynamic coupling of the extracellular matrix (ECM) to the cytoskeleton. This allows bidirectional transmission of forces between the ECM and the cytoskeleton, which tunes intracellular signaling cascades that control survival, proliferation, differentiation, and motility. The quantitative relationships between recruitment of distinct cell–matrix adhesion proteins and local cellular traction forces are not known. Here, we applied quantitative super-resolution microscopy to cell–matrix adhesions formed on fibronectin-stamped elastomeric pillars and developed an approach to relate the number of talin, vinculin, paxillin, and focal adhesion kinase (FAK) molecules to the local cellular traction force. We find that FAK recruitment does not show an association with traction-force application, whereas a ~60 pN force increase is associated with the recruitment of one talin, two vinculin, and two paxillin molecules on a substrate with an effective stiffness of 47 kPa. On a substrate with a fourfold lower effective stiffness, the stoichiometry of talin:vinculin:paxillin changes to 2:12:6 for the same ~60 pN traction force. The relative change in force-related vinculin recruitment indicates a stiffness-dependent switch in vinculin function in cell–matrix adhesions. Our results reveal a substrate-stiffness-dependent modulation of the relationship between cellular traction-force and the molecular stoichiometry of cell–matrix adhesions.

INTRODUCTION

Cell–matrix adhesions couple the intracellular cytoskeletal network to the extracellular matrix (ECM) and are key sites for bidirectional mechanotransduction.[1] First, they are the sites where cells apply myosin-driven contractile forces to their environment, for instance, during cell migration and tissue remodeling.[2] Second, they allow cells to sense and respond to changes in stiffness of their environment. The latter represents an important mechanical cue regulating stem cell differentiation, cancer progression, and various other processes in life and disease.[3–5]

Cell–matrix adhesions contain integrin transmembrane receptors that bind ECM components with their globular extracellular head domains. On the cytoplasmic side, integrins connect to a large complex of associated proteins with their intracellular tail domains. Integrins and integrin-associated proteins in cell–matrix adhesions have been demonstrated to change conformation, thereby exposing new interaction sites when stretched by force.[5] Several of the associated proteins, including talin and vinculin, connect the integrin cytoplasmic tails to the F-actin network.[6] Others, such as paxillin and focal adhesion kinase (FAK), are involved in local signaling platforms that regulate actin cytoskeletal dynamics, for instance, through Rho GTPases.[7] This allows cell–matrix adhesions to adjust their molecular architecture in response to force, ensuring a balance between extracellular (ECM) and intracellular forces.

Cell–matrix adhesions are highly dynamic structures.[8] Super-resolution microscopy techniques have been applied to reveal in detail the 3D multimolecular layered architecture of cell–matrix adhesions.[9,10] It is well known that larger cell–matrix adhesions support higher forces,[11–13] but quantitative relationships between recruitment of individual cell–matrix adhesion proteins and local traction-force application have not been reported. Here, we developed a novel method for the analysis of antibody-mediated direct stochastic optical reconstruction microscopy (dSTORM)[14] images.

For transformation of dSTORM data into local molecule-counting, we followed a real space approach making optimal use of the high positional accuracy characteristic of super-resolution imaging. We achieve this by using only the localization information and transform the cumulative distribution function of inter-localization distances (cdf) to absolute molecular numbers. This method has similarities to the number and brightness analysis known from correlation imaging,[15] mean shift clustering,[16] and the Fourier ring-correlation analysis method[17] and was inspired by colocalization statistics in single-molecule imaging.[18] We applied this novel method to four distinct cell–matrix adhesion components, such as talin, vinculin, paxillin, and FAK. The combination of dSTORM with traction-force microscopy allowed us to unravel quantitative relationships between their recruitment to cell–matrix adhesions and local traction forces.

For cells plated on a substrate with an effective Young's modulus of 47 kPa, we determined that the addition of one talin, vinculin, and paxillin molecule to a cell–matrix adhesion is accompanied by an, on average, 66, 30, and 32 pN increase in local traction-force, respectively. On a 12 kPa substrate, the stoichiometry for talin:vinculin:paxillin changes from 1:2:2 per ~60 nN force increment to ~2:12:6 for the same amount of traction force. Surprisingly, FAK recruitment did not significantly correlate with local traction force increase, irrespective of substrate rigidity. These findings provide a first quantitative relationship between recruitment of distinct cell–matrix adhesion proteins and local traction forces and reveal a remarkable regulation of the stoichiometry by substrate stiffness.

RESULTS

dSTORM on cell–matrix adhesion proteins

We analyzed the organization of vinculin in cell–matrix adhesions of vinculin knockout mouse embryonic fibroblasts transiently expressing green-fluorescent protein-tagged (GFP)-vinculin by confocal and super-resolution optical microscopy. Comparing signals derived from an Alexa-532-conjugated GFP nanobody to those from an Alexa-647-conjugated secondary antibody targeting a monoclonal vinculin antibody with confocal microscopy showed that these signals co-localized only in GFP positive cell–matrix adhesions as expected [Fig. 1(a), top, red arrows; i and ii]. As a control, cell–matrix adhesions in vinculin null MEFs lacking GFP-vinculin were readily identified using a paxillin antibody [Fig. 1(a), bottom, green arrows; (iii)] while such adhesions did not stain when the vinculin antibody was used Fig. 1(a), top].

Subsequently, we performed dSTORM and analyzed the overlap between fluorophore localizations for Alexa-532-conjugated GFP nanobody signals with vinculin monoclonal antibody followed by Alexa-647-conjugated secondary antibody signals in vinculin

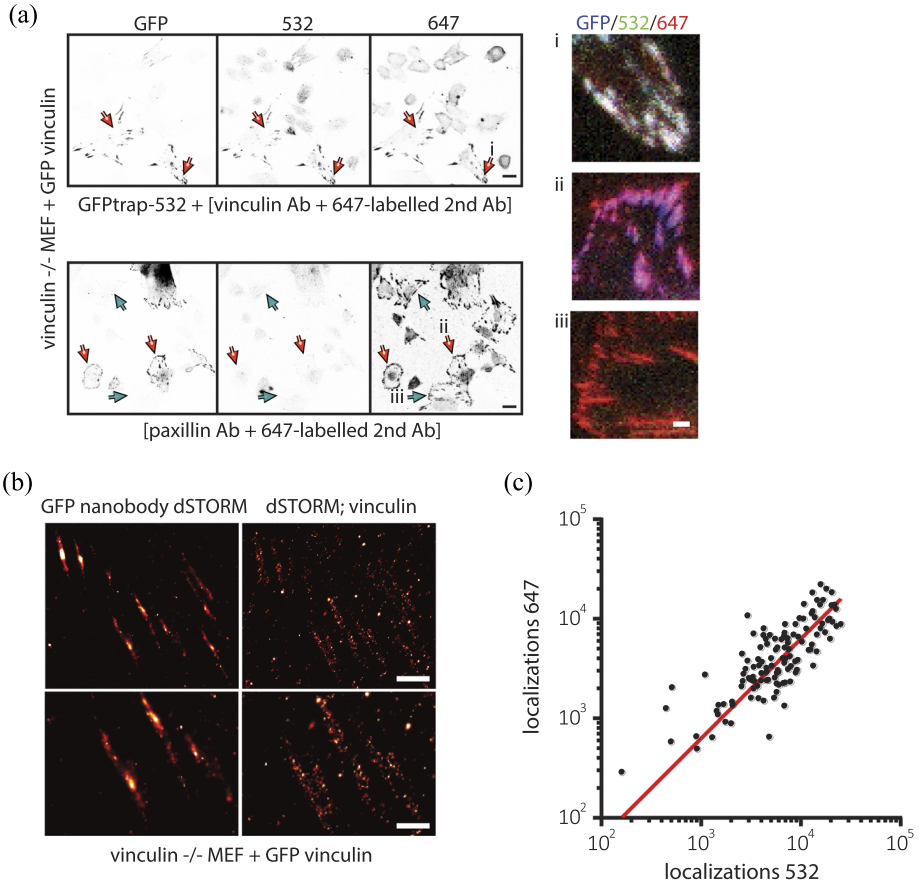

FIG. 1. dSTORM on cell–matrix adhesions. (a) Confocal images of vinculin −/− MEFs transiently expressing GFP vinculin, immunostained with the indicated antibodies. Red arrows indicate cells that are GFP (and vinculin) positive; green arrows indicate cells that are GFP (and vinculin) negative. In i, ii, and iii, merged images for the zoomed-in views of the indicated adhesions are shown. (b) Representative dSTORM images of cells immunostained with GFP nanobody conjugated with Alexa532 obtained with 532 nm laser (left) and (vinculin antibody plus secondary antibody conjugated with Alexa647) obtained with 647 nm laser (right). (c) Comparison of the number of localizations obtained from individual adhesions by applying dSTORM to first Alexa647 and then to Alexa532. The red line indicates the linear fit (R^2 = 0.47). Scale bars are 20 μm (a, left panels), 3 μm (a, right panels i–iii), 100 nm [(a), top], and 50 nm [(b), bottom].

null/GFP-vinculin cells. Samples were immersed in a switching-buffer, which leads to the quenching of the fluorescence with brief, infrequent de-quenching events resulting in images of sparse signal density <0.1 μm^{-2}. This permitted detection of signals from individual fluorophores on a sensitive camera (for details, see the section titled Materials and Methods). After localization of all fluorophores in each frame, the image of the cell–matrix adhesion structure was reconstructed from an image stack of 2×10^4 frames. dSTORM images, similar to confocal images, showed the predicted overlap between Alexa-532 and Alexa-647 localizations [Fig. 1(b)]. The number of localizations obtained from the two different fluorophores across 105 adhesions in 11 different cells as determined by dSTORM followed a linear dependence [Fig. 1(c)].

Combination of dSTORM and cellular traction force measurements

In order to combine force measurements and super-resolution microscopy, we seeded NIH3T3 fibroblasts on fibronectin stamped elastomeric micropillars. On these substrates, talin staining followed by confocal imaging identified cell–matrix adhesions coupled to fibronectin-stamped μ-pillars. The average background deflection, corresponding to the displacement resolution, was 50 ± 20 nm as determined by epi-fluorescence imaging in a cell-free region in the field of view of dSTORM imaging. For μ-pillar arrays with an effective Young's modulus of 12 or 47 kPa (spring constants per pillar of 16 or 66 nN/μm, respectively), the displacement resolution of 50 nm corresponded to a force precision of 0.8 and 3 nN, respectively. Combining epi-fluorescence pillar displacements and dSTORM provided simultaneous visualization of traction force and localizations in cell–matrix adhesions [Fig 2(a)]. The significant increase in spatial resolution between the dSTORM image and a wide-field image for a talin staining is apparent from Fig. 2(a). The resolution in the dSTORM image was largely determined by the positional accuracy by which each of the molecule was localized. We set the imaging conditions such that on average a signal of 520 photons per localization was detected [Figs. 2(a) and 2(c)]. At such a count rate, the localization precision was 14 ± 5 nm [Figs. 2(b) and 2(c)].

To reduce the cytoplasmic signal, we optimized a previously established permeabilization-during-fixation technique with the cytoskeleton buffer.[19] In order to confirm the force measurements in combination with dSTORM, we compared the measured forces to those obtained from live-cell experiments. We established that forces measured in samples fixed for dSTORM application were slightly lower than forces measured by live confocal imaging of pillar deflections in mCherry-LifeACT-labeled NIH3T3 cells [Figs. 2(d) and 2(e)]. The increase in force induced by seeding cells on a substrate with a higher effective Young's modulus as measured post-fixation recapitulated the increase measured in live cells, as established previously for fixation for standard immunofluorescence.[20] In accordance with the results obtained by confocal imaging, forces determined by epi-fluorescence microscopy in the field of view of dSTORM imaging of NIH3T3 cells that were immunostained for talin showed approximately threefold increase for cells seeded on 47 kPa as compared to forces applied by cells seeded on 12 kPa [Figs. 2(d)–2(f)].

From dSTORM localizations to molecule counts

We next investigated methods for obtaining molecule counts from dSTORM images. For photoactivation localization microscopy (PALM) where each protein of interest is fused to one fluorescent protein that bleaches fast and has very short dark times,[21] a cleaning algorithm can be used. This removes additional detections from the same fluorophore within the positional accuracy for single-molecule detection for a given time interval that safely exceeds the photobleaching time of the fluorophores. This method is susceptible to errors if the density of molecules exceeds the positional accuracy as may occur within cell–matrix adhesions and when multiple fluorophores per protein of interest are present as applies to dSTORM methods. Instead, for quantitative analysis of dSTORM data, density-based clustering algorithms are typically used where detections are categorized based on their local density as members of clusters.[22] Yet, also those methodologies are susceptible to errors due to local clustering of the proteins.

Here, we performed dSTORM mediated by two-step antibody staining with Alexa647 fluorophores on the secondary antibody that undergoes stochastic blinking.[14,23,24] In this design, signal amplification, as of binding of multiple secondary antibodies that all contain multiple fluorophores, will have to be accounted for in order to accurately estimate the true local stoichiometry. Therefore, we developed a method that makes use of the inherent high localization precision and signal amplification present in our setup. We based our methodology on analysis of the inter-localization distance distribution in the images, which, in turn, was used to distinguish between spatially correlated and uncorrelated localizations. Our novel method makes use of the fact that the statistics associated with fluorescence labeling and photophysics, although partly unknown, are equivalent for all spatially correlated and spatially uncorrelated localizations. Therefore, our method neither relies on the number of fluorophores per protein of interest, given there is enough signal amplification, nor does it depend on the photophysics of the fluorophores, as long as it remains constant during signal acquisition for one dSTORM image. Instead, our methodology uses solely the localization data. The methodology is able to quantify the number of molecules of any configuration as long as the molecular interspacing is larger than the positional accuracy, in the current case 14 ± 5 nm.

In order to estimate the number of talin molecules in an adhesion coupled to one pillar [Fig. 2(d), red box; Fig. 3(a)], we first manually selected the region associated with the adhesion(s) relating to one pillar. This selection was performed on the epi-fluorescence image by drawing a mask containing the cell–matrix adhesion extending from the pillar of interest in the direction of the deflection. This enabled the assessment of the molecular composition of the whole adhesion coupling a pillar to the actin cytoskeleton as it is known that these structures can "hang" from pillars.[13,25] We then determined the statistics for the cumulative distribution function of inter-localization distances (cdf) within the adhesion as shown in Fig. 3(b). For each distance, r, between two localizations, the number of distances smaller than r was determined as a function of the squared distance, r^2. For a spatially random distribution where the distances are uncorrelated, the distribution function increases linearly with r^2. In our data, the relationship between the cdf of inter-localization distances and r^2 displayed

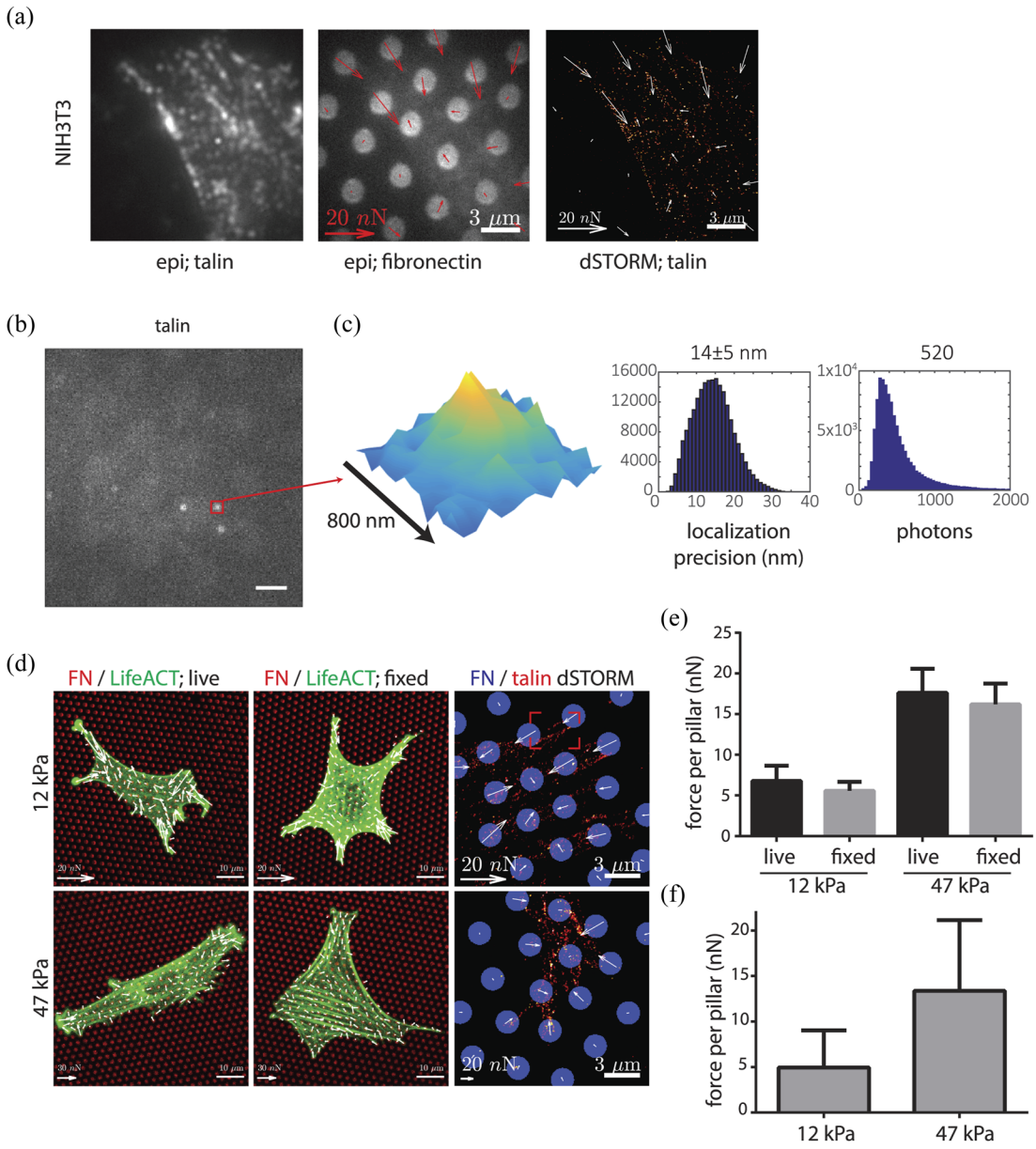

FIG. 2. Combination of dSTORM with micropillars. (a) NIH3T3 cell imaged with the dSTORM setup using epi-fluorescence with 647 (left) and 405 (middle) or dSTORM with 647 channel (right) together with accompanying force measurements (arrows in the middle and right images). (b) Example image frame from dSTORM acquisition with several Alexa647 molecules fluorescing. (c) Zoomed-in view of the red square in B (left) and histograms showing the positional accuracy of localizations from this dSTORM acquisition (left) and the intensity of localizations (right). (d) Images of live (left) and fixed (middle and right) NIH3T3 cells on pillars of an effective Young's modulus of 12 kPa (top) or 47 kPa (bottom) stamped with fibronectin conjugated to Alexa647 (left and middle) or Alexa405 (right). mCherry-LifeACT (left and middle) or talin immunostaining (right; secondary antibody conjugated with Alexa647) was imaged using confocal imaging (left and middle) or dSTORM setup (right) with calculated forces (arrows). (e) and (f) Bar graphs showing mean ± standard deviation of cellular forces applied per pillar calculated from confocal images (e) or images obtained with dSTORM setup (f) for cells on pillars with indicated stiffnesses. Scale bars are 3 μm [(a) and (d), right], 2 μm (b), and 10 μm [(d), left and middle]; deflection arrow scales are 20 nN [(a) and (d), top-right and bottom] and 30 nN [(d), top-left and top-middle].

two regimes. A linear regime was observed for large r^2, reflecting localizations belonging to uncorrelated, hence different talin molecules [Fig. 3(c)]. Subtracting this linear relationship from the data, the non-linear regime remained for small r^2 [Fig. 3(d)]. The non-linear initial increase reflects correlated detections, hence belonging to a single talin molecule or to a cluster of talin molecules. The non-linear regime was subsequently fit to a double exponential,

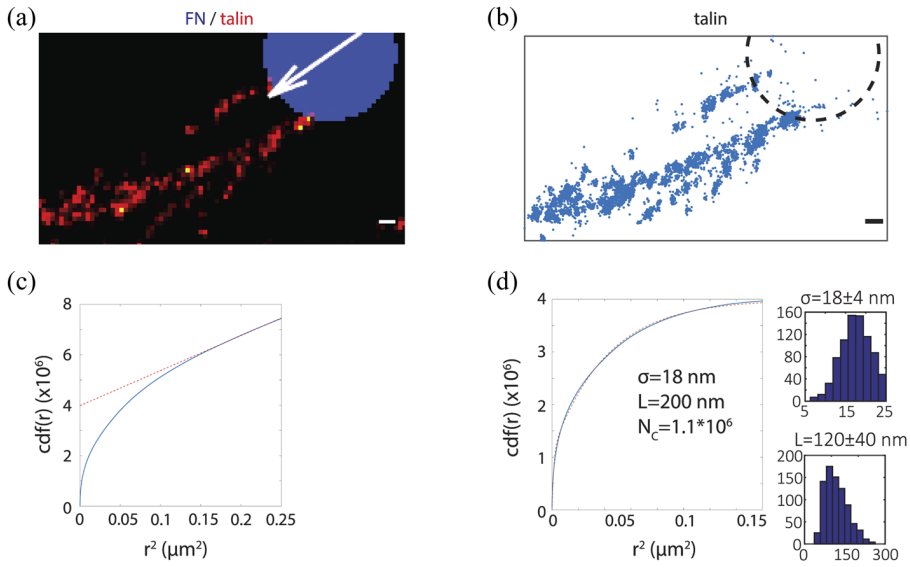

FIG. 3. Distribution analysis of talin dSTORM localizations in a single adhesion. (a) Zoomed-in view of the red square from Fig. 2(d). (b) Image derived from (a), showing 6700 localizations of Alexa647 targeted to talin associated with one pillar (dashed circle). (c) Cumulative distribution function of inter-localization distances (cdf) in B with a linear line fit (red dashed line) from 0.16 to 0.25 μm^2. (d) cdf from (c), with linear fit subtracted and accompanying double exponential fit $cdf(r) = N_c\left(1 - e^{-\frac{r^2}{4\sigma^2}}\right) + N_L\left(1 - e^{-\frac{r^2}{L^2}}\right)$ with σ = 18 nm, L = 200 nm, N_c = 1.10 × 10^6, and N_L = 2.9 × 10^6. Histograms of fit parameters σ (right-top) and L (right-bottom) obtained across all experiments are shown. Scale bars are 250 nm (a) and (b).

$$cdf(r) = N_c\left(1 - e^{-\frac{r^2}{4\sigma^2}}\right) + N_L\left(1 - e^{-\frac{r^2}{L^2}}\right), \quad (1)$$

where r denotes the distance between fluorophores, σ is the positional accuracy of position detections coupled to a single talin molecule, and N_c is the corresponding number of correlated distances. Furthermore, we added a second exponential that contains the information of the typical size of the focal adhesion, characterized by a typical length-scale L, and the number of localizations within this domain N_L, which is proportional to the number of talin molecules in close proximity. The structural length scale, L = (120 ± 40) nm, typical for adhesions, was considerably larger than the positional accuracy of talin localizations in dSTORM, σ = (18 ± 4) nm, indicating that the two components of the exponential were well separable. From the fit, the number of talin molecules N_m in the adhesion [Fig. 3(d)] was determined by (see the section titled Materials and Methods)

$$N_m = \frac{N^2}{(N + N_c)}, \quad (2)$$

where N is the total number of detections in the image. We validated the experimental strategy by simulations. We found an excellent agreement between the estimated number of molecules and our analysis: the accuracy was >90% even in conditions of high spatial overlap between individual signals [see Figs. 1(d)–1(f) of the supplementary material]. Using our methodology, 40 talin molecules were identified for the adhesion shown in Figs. 3(a) and 3(b). Since we calibrated our system and used fresh solutions for each experiment, we assume that fluorophore switching dynamics stay constant between different conditions. With sufficient signal amplification (>2000 localizations for 40 calculated molecules) and a much larger separation between the molecules compared to the localization precision (as calculated from the structural spacing length scale of 120 ± 40 nm in the talin experiments, being much larger than the localization scale of 18 ± 4 nm), the methodology renders reliable within our experimental setup. The sufficient signal amplification criterion was not met with the nanobody staining, and the quantification of the number of molecules was thus not carried out for the nanobody stainings in Fig. 1.

Relating the stoichiometry of cell–matrix adhesion proteins to traction forces

Having established a methodology to quantify the number of molecules in an adhesion, we studied the stoichiometry of four different cell–matrix adhesion proteins in cells seeded on pillar arrays of two different effective Young's moduli. In the analysis, cell–matrix adhesion areas were selected, and subsequently, the corresponding number of talin, vinculin, paxillin, and FAK molecules were calculated (see Fig. 2 of the supplementary material for histograms for all measurements and calculations). In order to relate the cell's force application to the number of adhesion molecules, we plotted the local traction force in relation to the number of detected molecules in an adhesion. In total, >100 cell–matrix adhesions from 30 NIH3T3 cells were analyzed in three independent experiments on μ-pillar arrays of an effective Young's modulus of 47 kPa. The data showed that the cellular force was highly correlated with the number of talin molecules in the respective adhesion [see Fig. 4(a) and the supplementary material (Fig. 3)]. Furthermore, the number of molecules and the force both increased with cell–matrix adhesion area (Fig. 3 of the supplementary material). Likewise, experiments performed on μ-pillar arrays of a lower effective Young's modulus (12 kPa) showed correlated talin–force relationships, yet forces applied by the adhesion per talin molecule were generally lower [see Fig. 4(b) and the supplementary material (Fig. 3)].

Similar to talin, the number of vinculin and paxillin molecules in a cell–matrix adhesion correlated with the cellular force application on both 47 and 12 kPa substrates (see Fig. 3 of the supplementary material). By contrast and to a surprise, the number of FAK molecules in an adhesion was not correlated with the

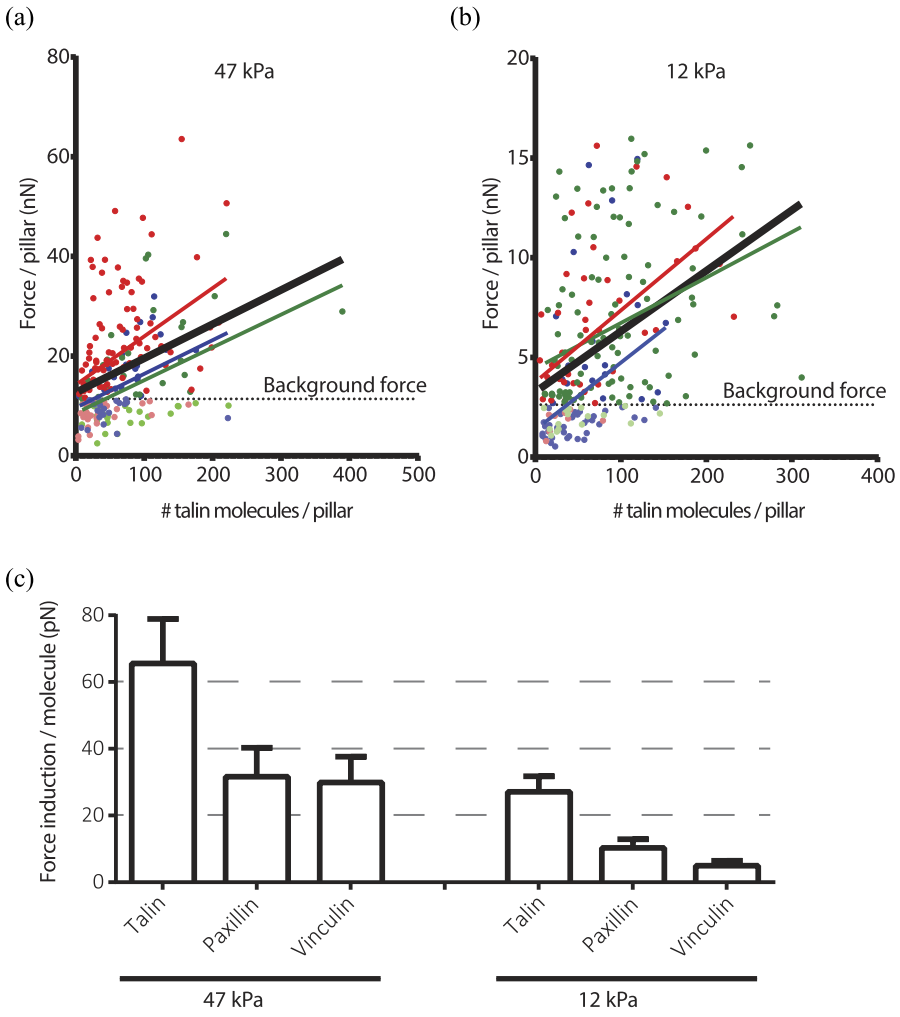

FIG. 4. Recruitment of talin, vinculin, and paxillin to cell–matrix adhesions is associated with distinct increments in forces that depend on substrate stiffness. (a) and (b) Measured force per cell–matrix adhesion plotted against the calculated number of talin molecules per adhesion for cells seeded on substrates with effective Young's moduli of 47 kPa (a) and 12 kPa (b). Dots indicate individual adhesions; lines indicate linear fits. Red, green, and blue colors represent data from three independent experiments. A solid black line represents linear fit for all data points from all three experiments. The dashed horizontal black line denotes the background forces measured. (c) Bar graphs showing linear fit slope values for the relationship between local traction force and the number of talin, paxillin, and vinculin molecules for cells seeded on substrates with effective Young's moduli of 47 and 12 kPa.

force application on neither of the substrates (see Fig. 3 of the supplementary material). For FAK, the number of molecules per area was uncorrelated to the traction force, indicating that the increased adhesion size rather than an increase in protein density was responsible for the increase in talin, vinculin, and paxillin molecules with increased force. For instance, irrespective of the amount of traction force measured, the numbers of talin molecules per square micrometer on 47 and 12 kPa pillars were 52 ± 3 and 54 ± 3, respectively.

Next, we quantified the correlations as a linear relationship between the abundance of talin, vinculin, and paxillin molecules in a cell–matrix adhesion to the local force application. We observed that both on the soft and stiff pillars, when the molecular abundance relationship is linearly approximated, this resulted in a non-zero force very close to our measured background forces [see Figs. 4(a) and 4(b) and the supplementary material (Fig. 3)]. It should be noted that here the background forces were quantified per image from the undeflected pillars, i.e., pillars outside of the cell, and the dotted line is the average background across all images. On a substrate with an effective Young's modulus of 47 kPa, for each additional talin molecule, an increase in the traction force by 66 pN was determined [Fig. 4(c)]. Vinculin and paxillin molecules were associated with about half of this force: for each additional vinculin and paxillin molecule, an increase in force by 30 pN and 32 pN was determined, respectively [Fig 4(c)]. On a substrate with an effective Young's modulus of 12 kPa, the force increments were less steep, with a stronger decrease in force association with vinculin was observed: 27 pN/talin, 4.9 pN/vinculin, and 10 pN/paxillin [Fig. 4(c)].

Together our findings indicate the following: (i) Talin, vinculin, and paxillin recruitment to cell–matrix adhesions is associated with distinct force increments. (ii) On a substrate of 47 kPa, an increase in local traction force of ~60 pN is accompanied by the recruitment of 1:2:2 talin:vinculin:paxillin molecules. (iii) On a four-times softer substrate, the force increments per molecule are less pronounced and vinculin-related force decreases dramatically. (iv) FAK recruitment is not significantly associated with the amount of local traction force.

DISCUSSION

Cell–matrix adhesions are highly dynamic multiprotein complexes that allow cells to sense and respond to physical cues from their surrounding ECM. We combined micropillar based traction force microscopy with super-resolution microscopy to obtain quantitative relationships between cell–matrix adhesion composition and local traction force. In order to address the number of molecules, we used the distribution of inter-localization distances in dSTORM images. Our methodology is independent of the fluorophore's photophysics that is at the core of intensity-based stoichiometry[26] but instead makes use of the high localization precision and signal amplification inherent to dSTORM imaging to quantify the number of molecules.

Previously, a probability density function calculated using Fourier space has been used to correct for multiple detections in PALM (PC-PALM).[27] Another method made use of Fourier ring correlation to relate the photophysics of detections outside of the structure of interest with the number of molecules inside this structure.[17] For either of these techniques to work, the labeling of a protein of interest with a single fluorophore is essential. This requires either precise genome editing or very accurate nanobody labeling. Both of these methods suffer from information loss due to discretization in Fourier space. By contrast, the method we developed here is real space based, taking full advantage of high localization precision. A very different approach was taken where photon arrival times were determined, and anti-bunching was analyzed to estimate the number of fluorophores present in a focal volume.[28,29] However, in contrast to our method, those approaches rely heavily on the detailed knowledge of the photophysics and, so far, less been used to count molecules.

Instead of trying to reach one fluorophore-per-molecule labeling, our methodology actually makes use of the high abundance of fluorophores per protein of interest and combines it with the high localization precision inherent to super-resolution methods. Our approach can be readily applied to commercially available antibodies in combination with labeled secondary antibodies used for standard immunostaining. A similar approach to ours was obtained through mean-shift clustering in real space to relate the number of localizations to the number of E-cadherin molecules.[16] The mean-shift clustering approach is computationally much more demanding and is more prone to potential artifacts caused by small deviations of the local stoichiometry. Making use of the cumulative distribution function of inter-localization distances we present here provides similar clustering information. Given our methodology relies on image correlation, all clusters associated with a complex are quantified as one entity, and it achieves a higher statistical significance and, thus, is less prone to error. Using this method, we reported here distinct force relationships for the cell–matrix adhesion proteins talin, vinculin, and paxillin that are modulated by environmental stiffness, whereas the recruitment of downstream FAK molecules was not related to the amount of local traction force (Fig. 5).

Similar to previous findings, we observed that larger cell–matrix adhesions support higher traction forces and that

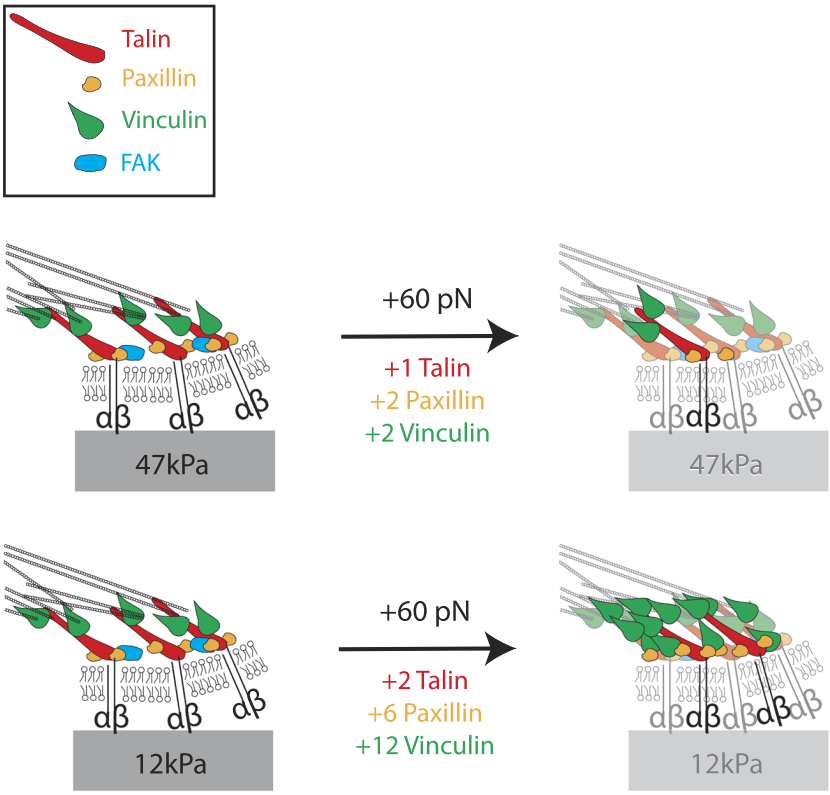

FIG. 5. Molecular composition of force responsive cell–matrix adhesions. Cartoon depicting recruitment of talin, paxillin, and vinculin molecules associated with a ~60 pN increase in force on stiff and soft substrates with the indicated effective Young's moduli.

adhesions with comparable areas can relate to a wide range of forces.[11–13] We additionally observed that adhesions with the same number of molecules can support a varying range of forces. Furthermore, we observed a non-zero y-intercept, suggesting a finite force in the absence of adhesion molecules, similar to the non-zero force reported at zero adhesion area.[11] However, this non-zero force is very close to the measured background forces. It should also be noted that, even though we do approximate the number of molecules–force relationship linearly, it is highly likely that the relationship is not linear. Indeed, nascent adhesions can exert a significant amount of forces with a non-linear intensity–traction relationship,[30] suggesting that the amount of force increase per molecule is much higher than our linear approximation estimates at nascent adhesions with low number of molecules.

Additionally, we found that the recruitment of talin, vinculin, or paxillin to the adhesion with increasing traction force was not accompanied by a significant change in molecule density. Rather, the increase in traction force was supported by the recruitment of cell–matrix adhesion proteins causing the adhesion to spatially expand. It has been reported that tension across individual talin molecules is largely constant over a wide range of substrate rigidities that trigger a range of cellular traction forces.[31] Together, these findings indicate that an increase in cellular traction force involves expansion of the adhesion through recruitment of new talin molecules without increasing the concentration of talin molecules or the force mediated by individual talin molecules.

Important to note that the increase in force associated with an additional talin, vinculin, or paxillin molecule that we report here does not represent the actual force exerted on these molecules but solely represents the overall force on the adhesion. Several additional cell–matrix adhesion proteins, which are not analyzed in our current study, are likely to be recruited to the growing adhesion as it applies more traction force. These include proteins that couple integrins to the cytoskeleton, such as α-actinin and filamin.[32] Their contribution has not been addressed here. As a single talin molecule interacts with a single integrin molecule, our finding that one additional talin molecule is associated with an additional 60 pN traction force on a 47 kPa substrate may point to an additional integrin being recruited to the adhesion with an increase in force. Alternatively, one pre-existing integrin may switch from interaction with filamin or α-actinin to interaction with the newly recruited talin molecule, as an additional 60 pN traction force is applied by the adhesion.

It has been reported that FAK is necessary for cellular traction force generation[33] and blocking myosin II activity impairs FAK recruitment to cell–matrix adhesions.[34] In that latter study, myosin activity was blocked with blebbistatin (20 μM), resulting in very small adhesions (0.17 μm^2). Here, we showed that FAK recruitment to cell–matrix adhesions does not correlate with increased traction forces on short or long pillars. This does not imply that FAK is not implicated in force generation. It has been shown that FAK activation through phosphorylation is force dependent[35] and, in turn, influences force-dependent phosphorylation of paxillin and recruitment of vinculin.[34] It should be noted the number of molecules we observed for FAK was the lowest among all proteins quantified. Since for FAK quantification, we obtained the necessary signal amplification (1050 ± 1300 localizations for 34 ± 31 molecules on stiff and 880 ± 760 localizations for 38 ± 34 molecules on soft pillars; see Fig. 2 of the supplementary material) and a much larger separation between molecules than our localization precision (100 ± 34 ≫ 17 ± 3 nm for stiff pillars and 92 ± 33 ≫ 16 ± 4 nm for soft pillars, data not shown), and we do not expect this to be an artifact of our methodology. However, while our method relies on the antibodies used, and subsequently all molecular quantifications, including FAK, do depend on the efficiency of the staining, this is constant across our experiments. Therefore, the force/molecule relationship, especially the lack thereof we observe for FAK, should be truthful.

A recent publication has shed some light on the relation of FAK abundance and activity to force application.[36] It was demonstrated that the integrated fluorescence signal for both total FAK and phosphorylated FAK scaled linearly with the applied force for micropillars of 14 kPa stiffness. No correlation was found for pillars of 5 kPa stiffness. While we do see larger areas for higher forces on both of our tested stiffnesses, also in the total FAK stainings (data not shown), this is not accompanied by a higher number of FAK molecules. Together, both findings indicate that the FAK density decreases with increasing force. This is also evident from the fact that the range of the integrated signal strength reported by Zhou *et al.* did not change between 5 and 14 kPa substrates, while the forces measured more than doubled.[36] Our findings, together with studies showing that FAK residence times are low and increase with increasing cell–matrix adhesion size,[34,37] suggest that changes in FAK activity rather than its recruitment are coupled to force. The relationship between relative phosphorylation of FAK (phosphorylated FAK:total FAK ratio) and force might be able to clearly answer if FAK activity is force-dependent.

We find that the stoichiometry of talin molecules in cell–matrix adhesions is associated with the highest traction forces on stiff as well as softer substrates as compared to vinculin and paxillin. On a stiff substrate, an increase in traction force of ~60 pN is associated with one additional talin molecule, whereas two additional vinculin and paxillin molecules are associated with the same force increase (Fig. 5). Talin connects the integrin to actin and acts as a scaffold for vinculin binding.[31,38] The binding of talin to the integrin cytoplasmic tail activates the integrin and enhances ECM binding, and the interaction of talin with integrin $\alpha v\beta 3$ is important for adhesion strengthening.[39] Forces on talin molecules open cryptic binding sites for vinculin.[40] It has been shown that induction of myosin contractility triggers this unfolding, which is also correlated with more actin proximal localization of vinculin and adhesion maturation.[10] Furthermore, vinculin binds to talin in live cells in a force-dependent manner[41] and forces transduced by individual talin molecules are reduced in the absence of vinculin but not entirely lost.[31] This is possibly due to force-induced stabilization of vinculin in adhesions[42] and force stabilization within adhesions,[43] which both depend on the interaction of vinculin with actin and talin. These findings indicate that the recruitment of talin and vinculin, as well as their interaction, is important for force-related adhesion maturation. As described above, vinculin can also be recruited to cell–matrix adhesions through FAK-mediated phosphorylation of paxillin, a process that depends on myosin-mediated contractility.[10,34]

Experiments on isolated talin molecules have shown that cryptic vinculin binding sites become available when talin is under 5–25 pN tension.[44] The 66 or 27 pN increase in traction force we measure for a cell–matrix adhesion on a stiff or soft substrate, respectively,

per additional talin molecule is beyond the reported threshold for opening vinculin binding sites and below the 100 pN forces that can be supported by single actin molecules.[45] Additionally, it has been demonstrated that adhesions containing paxillin and vinculin can form without talin, but these adhesions demonstrate hindered force application.[46] Notably, vinculin molecules that are recruited to the adhesion via talin, phospho-paxillin, or other interactions, such as force-dependent p130Cas-vinculin binding,[47] may partially remain in an inactive conformation, especially on a soft substrate, which may explain the lower force induction measured for each recruited vinculin molecule as compared to talin. Indeed, simulations have shown that vinculin can be in two different configurations depending on the amount of force across the molecule, both of which can interact with talin, and the switching happens at about 30 pN,[48] which is the recruitment force we measure on 47 kPa substrates.

Interestingly, it has been reported that as adhesions enlarge, forces on individual vinculin molecules decrease.[49] In addition, a switch behavior has been demonstrated for vinculin: for very small and very large adhesions, tension on vinculin adhesion growth is slowed, while for adhesions of intermediate size, a positive correlation of vinculin tension with adhesion growth was found.[50] The fact that vinculin exhibits a slow turnover in cell–matrix adhesions on glass and that inhibition of myosin contractility raises its turnover to that observed for other cell–matrix adhesion proteins further suggests that vinculin changes its function with force.[34,51] Our findings extend these observations, showing that a decrease in substrate rigidity leads to a major decrease in vinculin-associated force, i.e., for the same amount of force increase, the number of recruited vinculin molecules is six times higher on a soft vs a stiff substrate (Fig. 5). This suggests that the activation of vinculin molecules is less efficient on a low rigidity substrate, rendering a pool of vinculin molecules in an inactive state. Vinculin activation is proposed to occur through its interaction with talin.[10] Larger forces applied on stiff substrates in our experiments may enhance the talin–vinculin interaction, thereby more effectively supporting vinculin activation and subsequent coupling of vinculin to the actin cytoskeleton.

Taken together, we have combined dSTORM and traction-force microscopy to obtain quantitative information on the relationship between the molecular composition of cell–matrix adhesions and their force application. We report that an increase in the force of ~60 pN is accompanied by the recruitment of 1:2:2 talin:vinculin:paxillin proteins on a substrate with an effective stiffness of 47 kPa (Fig. 5). The stoichiometry changes on softer substrates, in particular, due to a strong reduction of vinculin-associated force. The methodology we introduced here for extraction of quantitative molecular information from super-resolution images is readily applicable to other cellular structures given that there is enough signal amplification, i.e., multiple fluorophores associated with the protein of interest and/or multiple blinking events are observed per fluorophore.

MATERIALS AND METHODS

Cell culture and transduction

Vinculin KO MEFs (kindly provided by Dr. Johan de Rooij, Utrecht University, NL) and NIH-3T3 fibroblasts were cultured in medium (DMEM; Dulbecco's modified Eagle's Medium, Invitrogen/Fisher Scientific) supplemented with 10% newborn calf serum, 25 U/ml penicillin, and 25 μg/ml streptomycin (Invitrogen/Fisher Scientific Cat. No. 15070-063). Vinculin KO MEFs were transduced with a GFP-vinculin retroviral construct as previously described.[52]

Micropillar preparation and cell seeding

Micropillar arrays were used for cellular traction force measurements according to the methodology described previously.[13] A negative silicon master was made with 10 × 10 mm arrays of circular holes of 4.1 or 6.9 μm depth, 2 μm diameter, and 4 μm center-to-center distance in a hexagonal grid with two rectangular spacers of 10 × 2 mm^2 wide and 50 μm high aligned on the sides of the arrays using a two-step Deep Reactive Ion Etching (DRIE) process. The negative silicon master was passivated with trichlorosilane (Sigma-Aldrich) and well-mixed polydimethylsiloxane (PDMS) at 1:10 ratio (crosslinker:prepolymer) was poured over the wafer and cured for 20 h at 110 °C. Pillar arrays of 4.1 and 6.9 μm height had a bending stiffness of 66 and 16 nN/μm, respectively, corresponding to an effective Young's modulus, E_{eff}, of 47.2 and 11.6 kPa, respectively[20] Stamping of fibronectin was performed using a flat piece of PDMS (1:30 ratio, cured 16 hours at 65 °C) that had been incubated with a mix of 50 μg/ml unlabeled fibronectin (Sigma-Aldrich) and 10 μg/ml Alexa405 or Alexa647 (both from Invitrogen)-conjugated fibronectin. Subsequently, the stamped micropillars were blocked with 0.2% Pluronic (F-127, Sigma-Aldrich), and cells were seeded at single-cell density in complete medium and incubated for 5 hours at 37 °C and 5% CO_2.

Fixation and immunostaining

Samples were washed once with cytoskeleton buffer (CB) (10 mM MES, 150 mM NaCl, 5 mM EGTA, 5 mM $MgCl_2$, and 5 mM glucose),[19] fixed and permeabilized for 10 s with 0.1%–0.25% Triton-X, 0.4% paraformaldehyde, and 1 μg/ml phalloidin in CB, fixed for 10 min with 4% formaldehyde in CB, permeabilized for 10 min with 0.5% Triton-X, and blocked for 30 min with 0.5% BSA. Immunostaining was performed with an Alexa-532-conjugated GFP nanobody (Chromotek, Germany) or with a primary mouse monoclonal antibody against talin (Sigma, T-3287), FAK (BD Transduction, 610087), paxillin (BD Transduction, 610052), or vinculin (Sigma, V-9131), followed by an Alexa647-conjugated secondary antibody against mouse IgG (Jackson, 115-605-006) following the protocol suggested by van de Linde *et al.*[14]

Imaging and analysis

dSTORM imaging

Super-resolution imaging was performed on a home-built wide-field single-molecule setup, based on an Axiovert S100 (Zeiss) inverted microscope equipped with a 100×1.4NA oil-immersion objective (Zeiss, Germany). Micropillar arrays were inverted onto #0 thickness, 25 mm diameter, and round coverslips (Menzel Glaser). Imaging was performed in 100 mM mercaptoethylamine (MEA, Sigma-Aldrich) in PBS. A 405 nm laser (CrystaLaser, USA) was used for imaging the pillars and photoswitching of the Alexa647 dye to adjust the density of visible fluorophores. The light was reflected

into the objective by a dichroic mirror (ZT405/532/635rpc, Chroma, USA). The fluorescence light in the detection path was filtered using the emission filter ZET532/633m (Chroma, USA). Conversion intensities were set between 0 and 250 W/cm^2 at 405 nm, and the excitation intensity was set to 5 kW/cm^2 at 647 nm. For each sample, we acquired 20 000 images with an acquisition time of 10 ms per frame at a frame rate of 69 Hz. The signal of individual dye molecules was captured on a sCMOS Orca Flash 4.0V2 camera (Hamamatsu, Japan). The average integrated signal of a single fluorophore was 520 detected photons, spatially distributed by the point-spread function of the microscope of 440 nm FWHM, resulting in a sigma of 187 nm in a Gaussian approximation.

The signal from individual fluorophores was fitted with a 2-dimensional Gaussian using a custom least-squares algorithm in Matlab.[53] From the fit, we determined the location of each fluorophore to an accuracy of 14 ± 5 nm [Fig. 3(b)]. This localization accuracy is slightly higher than its theoretical minimum predicted from the width of the point-spread function and the detected signal, 187 nm/$\sqrt{[520]}$ = 8.2 nm.

Obtaining and fitting the cumulative distribution function of inter-localization distances (cdf)

The area of interest from the epi-fluorescence image was obtained by manually drawing a mask containing the cell–matrix adhesion extending from the pillar of interest in the direction of the deflection. Localizations corresponding to blinking events in this area were analyzed [Figs. 3(a) and 3(b)]. From the position data, the two-point spatial correlation function g(r) and subsequently the cumulative distribution function of inter-localization distances (cdf) were calculated,

$$cdf(r) = \int_0^r g(r')dr'. \tag{3}$$

For discrete 2D position data $r_i = \{x_i, y_i\}$, as obtained from the fits, the cdf was constructed as

$$cdf(r) = 2\sum_{i=1}^{N}\sum_{j=i+1}^{N}(x_i - x_j)^2 + (y_i - y_j)^2 < r^2. \tag{4}$$

The cdf describes the number of distances that are smaller than r, in a sample of N localizations.

The positional accuracy leads to an apparent Gaussian spread in the localization of an individual molecule characterized by a cdf,

$$cdf(r) = N_c\left(1 - e^{-\frac{r^2}{4\sigma^2}}\right), \tag{5}$$

with correlation length, σ_i, given by a combination of the localization uncertainty for an individual fluorophore and the size of a primary and secondary antibody complex used to label the protein of interest. Both detection and labeling originate from statistical processes. Here, N_c is the total number of correlated distances and σ is the mean positional uncertainty for all localizations coupled to one protein of interest. Equation (5) is valid for $r \sim \sigma$.

On length scales longer than the correlation length, the cdf was characterized by a distance distribution for uncorrelated localizations. Assuming a homogeneous, random organization of localizations within a given field-of-view of area, A, the cdf follows a quadratic dependence on distance as

$$cdf(r) = N_u\frac{\pi r^2}{A}, \tag{6}$$

where N_u is the number of uncorrelated distances.

Thus, the general form for the spatial correlation function was a linear combination of the correlated and the uncorrelated part,

$$cdf(r) = N_c\left(1 - e^{-\frac{r^2}{4\sigma^2}}\right) + N_u\frac{\pi r^2}{A}. \tag{7}$$

Running a simulation on 2048 individual molecules randomly positioned in a box of 2 × 2 μm^2, each detected by 100 localizations at a positional accuracy of 20 nm [see Fig. 1(d) of the supplementary material], the distance distribution was calculated and its dependence on the squared distance, r^2, is shown [see Fig. 1(e) of the supplementary material]. For squared distances beyond 4×10^{-3} μm^2, the cdf(r) became linearly dependent on r^2 with the slope of $\pi N_u/A$ and y-intersect at $N_c(2 \times 10^4)$ as predicted.

Calculation of number of molecules from the fit

From N_c, the number of molecules was calculated as follows: The number of localizations, N, originating from N_m molecules each being observed n_i times is given by

$$N = \sum_{i=1}^{N_m} n_i = N_m\langle n\rangle, \tag{8}$$

where <n> is the average number of observations per molecule. Hence, $N^2 = (N_m\langle n\rangle)^2$.

Likewise, the total number of correlated distances, N_c per molecule is given by $n_i \times (n_i - 1)$. For all molecules, this yields

$$N_c = \sum_{i=1}^{N_m}\left(n_i^2 - n_i\right) = (N_m)^2\langle n^2\rangle N. \tag{9}$$

Therefore,

$$\frac{N^2}{N_c + N} = \frac{(N_m\langle n\rangle)^2}{(N_m)^2\langle n^2\rangle}. \tag{10}$$

Rearranging gives

$$N_m = \frac{N^2}{N_c + N}\cdot\left(1 + \frac{var(n)}{\langle n^2\rangle}\right), \tag{11}$$

where $var(n) = \langle n^2\rangle - \langle n\rangle^2$ is the variance in the number of detections per molecule. The second term, $\left(1 + \frac{var(n)}{\langle n^2\rangle}\right)$, summarizes the properties of the joined statistics of labeling and photophysics of the fluorophores and its value varies between 1 and 2, depending on which of the various processes dominate the joined statistics and for a typical dSTORM experiment is close to one (see the supplementary material for a more detailed analysis).

Simulations were performed for densities between 40 and 4000 randomly distributed molecules on an area of 2 × 2 μm^2. 100 localizations per molecule were simulated with a mean positional accuracy σ = 20 nm. At high densities, there was a significant overlap of molecules within the image [see Fig. 1(d) of the supplementary material]. The number of estimated molecules faithfully followed the input within an error of <10% [see Fig. 1(f) of the supplementary material].

Estimation of the number of molecules in an adhesion

In the quantification of the number of correlated distances, it was assumed that all molecules were randomly organized, which is not the case for molecule clusters such as present in a cell–matrix adhesion. This restriction is readily lifted by the addition of a second exponential term with weight, N_L that accounts for a length scale, and L that characterizes any spatial structures in real data. In this case, the cdf for a nonlinear regime becomes

$$cdf(r) = N_c\left(1 - e^{-\frac{r^2}{4\sigma^2}}\right) + N_L\left(1 - e^{-\frac{r^2}{L^2}}\right). \quad (12)$$

For the distinction of the two components, the typical structural length scale should be significantly larger than the positional accuracy, $L > 4\sigma$, typically 40 nm for a positional accuracy of 10 nm. The structure parameter of adhesion clustering measured here was way above this threshold, L = 120 ± 40 nm. Hence, the method described above provides a very general solution for molecule counting in super-resolution microscopy, where

$$N_m = \frac{N^2}{N_c + N} \cdot \left(1 + \frac{var(n)}{\langle n^2 \rangle}\right). \quad (13)$$

Deflection analysis

Pillar deflections were determined at ~50 nm precision using a specifically designed Matlab script. The pillar locations were determined from the labeled fibronectin fluorescence images using a fit to the cross-correlation function between a perfect binary circle and the local fluorescence of one pillar. Those positions were compared to those of a perfect hexagonal grid used as reference. From an undeflected array image, the accuracy was found to be 47.1 nm [see Figs. 1(b) and 1(c) of the supplementary material], which corresponds to a force accuracy of 780 pN and 3.1 nN on the pillar array of E_{eff} = 11.6 kPa and 47.2 kPa, respectively. Masks for adhesions corresponding to individual pillars of interest were manually drawn for each case.

Statistical analysis

p-values were calculated using the F-test for linear regression analysis using GraphPad Prism 6.0.

SUPPLEMENTARY MATERIAL

See the supplementary material for supplementary Figs. 1–3, cdf calculations, and estimation of coefficient-of-variation for number of detections per molecule (relating to term $var(n) = \langle n^2 \rangle - \langle n \rangle^2$), and a simulation for the combined statistics with secondary antibody labeling.

ACKNOWLEDGMENTS

We thank Dr. Johan de Rooij (Utrecht University, NL) for kindly providing cells and Dr. Hedde van Hoorn (VU University, NL) for his assistance with pillar deflection analysis. This work was financially supported by the Netherlands Organization for Scientific Research (Grant No. FOM 09MMC03).

AUTHOR DECLARATIONS

Conflict of Interest

The authors have no conflicts to disclose.

Author Contributions

H.E.B. and R.H. contributed equally to this work.

DATA AVAILABILITY

The data that support the findings of this study are available from the corresponding authors upon reasonable request.

REFERENCES

[1] K. A. Jansen *et al.*, "A guide to mechanobiology: Where biology and physics meet," Biochim. Biophys. Acta, Mol. Cell Res. **1853**, 3043–3052 (2015).
[2] E. Papusheva and C.-P. Heisenberg, "Spatial organization of adhesion: Force-dependent regulation and function in tissue morphogenesis," EMBO J. **29**, 2753–2768 (2010).
[3] S. Kumar and V. M. Weaver, "Mechanics, malignancy, and metastasis: The force journey of a tumor cell," Cancer Metastasis Rev **28**, 113–127 (2009).
[4] A. Buxboim, I. L. Ivanovska, and D. E. Discher, "Matrix elasticity, cytoskeletal forces and physics of the nucleus: How deeply do cells 'feel' outside and in?," J. Cell Sci. **123**, 297–308 (2010).
[5] S. W. Moore, P. Roca-Cusachs, and M. P. Sheetz, "Stretchy proteins on stretchy substrates: The important elements of integrin-mediated rigidity sensing," Dev. Cell **19**, 194–206 (2010).
[6] C. Brakebusch and R. Fässler, "The integrin-actin connection, an eternal love affair," EMBO J. **22**, 2324–2333 (2003).
[7] S. Huveneers and E. H. J. Danen, "Adhesion signaling–crosstalk between integrins, Src and Rho," J. Cell Sci. **122**, 1059–1069 (2009).
[8] J. T. Parsons, A. R. Horwitz, and M. A. Schwartz, "Cell adhesion: Integrating cytoskeletal dynamics and cellular tension," Nat. Rev. Mol. Cell Biol. **11**, 633–643 (2010).
[9] P. Kanchanawong *et al.*, "Nanoscale architecture of integrin-based cell adhesions," Nature **468**, 580–584 (2010).
[10] L. B. Case *et al.*, "Molecular mechanism of vinculin activation and nanoscale spatial organization in focal adhesions," Nat. Cell Biol. **17**, 880–892 (2015).
[11] L. Trichet *et al.*, "Evidence of a large-scale mechanosensing mechanism for cellular adaptation to substrate stiffness," Proc. Natl. Acad. Sci. U. S. A. **109**, 6933–6938 (2012).
[12] N. Q. Balaban *et al.*, "Force and focal adhesion assembly: A close relationship studied using elastic micropatterned substrates," Nat. Cell Biol. **3**, 466–472 (2001).
[13] H. van Hoorn *et al.*, "The nanoscale architecture of force-bearing focal adhesions," Nano Lett. **14**, 4257–4262 (2014).
[14] S. van de Linde *et al.*, "Direct stochastic optical reconstruction microscopy with standard fluorescent probes," Nat. Protoc. **6**, 991–1009 (2011).
[15] M. A. Digman, R. Dalal, A. F. Horwitz, and E. Gratton, "Mapping the number of molecules and brightness in the laser scanning microscope," Biophys. J. **94**, 2320–2332 (2008).
[16] Y. Wu, P. Kanchanawong, and R. Zaidel-Bar, "Actin-delimited adhesion-independent clustering of E-cadherin forms the nanoscale building blocks of adherens junctions," Dev. Cell **32**, 139–154 (2015).

[17]R. P. J. Nieuwenhuizen *et al.*, "Quantitative localization microscopy: Effects of photophysics and labeling stoichiometry," PLoS One **10**, e0127989 (2015).
[18]W. Trabesinger *et al.*, "Statistical analysis of single-molecule colocalization assays," Anal. Chem. **73**, 1100–1105 (2001).
[19]J. Prast, M. Gimona, and J. Small, "Immunofluorescence microscopy of the cytoskeleton: Combination with green fluorescent protein tags," Cell Biol. **1**, 557–561 (2006).
[20]H. E. Balcioglu, H. van Hoorn, D. M. Donato, T. Schmidt, and E. H. J. Danen, "The integrin expression profile modulates orientation and dynamics of force transmission at cell–matrix adhesions," J. Cell Sci. **128**, 1316–1326 (2015).
[21]P. Annibale, S. Vanni, M. Scarselli, U. Rothlisberger, and A. Radenovic, "Quantitative photo activated localization microscopy: Unraveling the effects of photoblinking," PLoS One **6**, e22678 (2011).
[22]N. Ehmann *et al.*, "Quantitative super-resolution imaging of Bruchpilot distinguishes active zone states," Nat. Commun. **5**, 4650 (2014).
[23]M. Heilemann *et al.*, "Subdiffraction-resolution fluorescence imaging with conventional fluorescent probes," Angew. Chem. Int. Ed. **47**, 6172–6176 (2008).
[24]D. Baddeley, I. D. Jayasinghe, C. Cremer, M. B. Cannell, and C. Soeller, "Light-induced dark states of organic fluochromes enable 30 nm resolution imaging in standard media," Biophys. J. **96**, L22–L24 (2009).
[25]B. L. Doss *et al.*, "Cell response to substrate rigidity is regulated by active and passive cytoskeletal stress," Proc. Natl. Acad. Sci. U. S. A. **117**, 12817–12825 (2020).
[26]T. Schmidt, G. J. Schütz, H. J. Gruber, and H. Schindler, "Local stoichiometries determined by counting individual molecules," Anal. Chem. **68**, 4397–4401 (1996).
[27]P. Sengupta *et al.*, "Probing protein heterogeneity in the plasma membrane using PALM and pair correlation analysis," Nat. Methods **8**, 969–975 (2011).
[28]J. Sýkora *et al.*, "Exploring fluorescence antibunching in solution to determine the stoichiometry of molecular complexes," Anal. Chem. **79**, 4040–4049 (2007).
[29]H. Ta *et al.*, "Mapping molecules in scanning far-field fluorescence nanoscopy," Nat. Commun. **6**, 7977 (2015).
[30]K. A. Beningo, M. Dembo, I. Kaverina, J. V. Small, and Y.-l. Wang, "Nascent focal adhesions are responsible for the generation of strong propulsive forces in migrating fibroblasts," J. Cell Biol. **153**, 881–888 (2001).
[31]K. Austen *et al.*, "Extracellular rigidity sensing by talin isoform-specific mechanical linkages," Nat. Cell Biol. **17**, 1597–1606 (2015).
[32]A.-X. Zhou, J. H. Hartwig, and L. M. Akyürek, "Filamins in cell signaling, transcription and organ development," Trends Cell Biol. **20**, 113–123 (2010).
[33]B. Fabry, A. H. Klemm, S. Kienle, T. E. Schäffer, and W. H. Goldmann, "Focal adhesion kinase stabilizes the cytoskeleton," Biophys. J. **101**, 2131–2138 (2011).
[34]A. M. Pasapera, I. C. Schneider, E. Rericha, D. D. Schlaepfer, and C. M. Waterman, "Myosin II activity regulates vinculin recruitment to focal adhesions through FAK-mediated paxillin phosphorylation," J. Cell Biol. **188**, 877–890 (2010).
[35]J. Seong *et al.*, "Distinct biophysical mechanisms of focal adhesion kinase mechanoactivation by different extracellular matrix proteins," Proc. Natl. Acad. Sci. U. S. A. **110**, 19372–19377 (2013).
[36]D. W. Zhou *et al.*, "Force-FAK signaling coupling at individual focal adhesions coordinates mechanosensing and microtissue repair," Nat. Commun. **12**, 2359 (2021).
[37]S. E. Le Dévédec *et al.*, "The residence time of focal adhesion kinase (FAK) and paxillin at focal adhesions in renal epithelial cells is determined by adhesion size, strength and life cycle status," J. Cell Sci. **125**, 4498–4506 (2012).
[38]S. Tadokoro *et al.*, "Talin binding to integrin ß tails: A final common step in integrin activation," Science **302**, 103–106 (2003).
[39]P. Roca-Cusachs, N. C. Gauthier, A. Del Rio, and M. P. Sheetz, "Clustering of $\alpha_5\beta_1$ integrins determines adhesion strength whereas $\alpha_v\beta_3$ and talin enable mechanotransduction," Proc. Natl. Acad. Sci. U. S. A. **106**, 16245–16250 (2009).
[40]A. del Rio *et al.*, "Stretching single talin rod molecules activates vinculin binding," Science **323**, 638–641 (2009).
[41]H. Hirata, H. Tatsumi, C. T. Lim, and M. Sokabe, "Force-dependent vinculin binding to talin in live cells: A crucial step in anchoring the actin cytoskeleton to focal adhesions," Am. J. Physiol. Cell Physiol. **306**, C607–C620 (2014).
[42]K. E. Rothenberg, D. W. Scott, N. Christoforou, and B. D. Hoffman, "Vinculin force-sensitive dynamics at focal adhesions enable effective directed cell migration," Biophys. J. **114**, 1680–1694 (2018).
[43]R. Tapia-Rojo, A. Alonso-Caballero, and J. M. Fernandez, "Direct observation of a coil-to-helix contraction triggered by vinculin binding to talin," Sci. Adv. **6**, eaaz4707 (2020).
[44]M. Yao *et al.*, "Mechanical activation of vinculin binding to talin locks talin in an unfolded conformation," Sci. Rep. **4**, 4610 (2015).
[45]A. Kishino and T. Yanagida, "Force measurements by micromanipulation of a single actin filament by glass needles," Nature **334**, 74–76 (1988).
[46]P. Atherton *et al.*, "Relief of talin autoinhibition triggers a force-independent association with vinculin," J. Cell Biol. **219** (2020).
[47]R. Janoštiak *et al.*, "CAS directly interacts with vinculin to control mechanosensing and focal adhesion dynamics," Cell. Mol. Life Sci. **71**, 727–744 (2014).
[48]L. Sun, J. K. Noel, H. Levine, and J. N. Onuchic, "Molecular simulations suggest a force-dependent mechanism of vinculin activation," Biophys. J. **113**, 1697–1710 (2017).
[49]C. Grashoff *et al.*, "Measuring mechanical tension across vinculin reveals regulation of focal adhesion dynamics," Nature **466**, 263–266 (2010).
[50]P. Hernández-Varas, U. Berge, J. G. Lock, and S. Strömblad, "A plastic relationship between vinculin-mediated tension and adhesion complex area defines adhesion size and lifetime," Nat. Commun. **6**, 7524 (2015).
[51]H. Wolfenson, A. Bershadsky, Y. I. Henis, and B. Geiger, "Actomyosin-generated tension controls the molecular kinetics of focal adhesions," J. Cell Sci. **124**, 1425–1432 (2011).
[52]E. H. J. Danen *et al.*, "Integrins control motile strategy through a Rho–cofilin pathway," J. Cell Biol. **169**, 515–526 (2005).
[53]T. Schmidt, G. J. Schutz, W. Baumgartner, H. J. Gruber, and H. Schindler, "Imaging of single molecule diffusion," Proc. Natl. Acad. Sci. U. S. A. **93**, 2926–2929 (1996).